A new approach to mapping landslide hazards: a probabilistic integration of empirical and physically-based models in the North Cascades of Washington, U.S.A.

Ronda Strauch[1], Erkan Istanbulluoglu[2], and Jon Riedel[3]

1. Seattle City Light, Seattle, WA and Civil and Environmental Engineering, University of

Washington, Seattle, WA

2. Civil and Environmental Engineering, University of Washington, Seattle, WA

3. National Park Service, US Dept. of Interior, Sedro-Woolley, WA

Corresponding author:

Ronda Strauch
Seattle City Light
700 5th Ave #3316, Seattle, WA 98124
Tel: 425-445-7934
E-mail: ronda.strauch@seattle.gov

Abstract

We developed a new approach for mapping landslide hazard by combining probabilities of
landslide impact derived from a data-driven statistical approach and a physically-based model of
shallow landsliding. Our statistical approach integrates the influence of seven site attributes on
observed landslides using a frequency ratio method. Influential attributes and resulting
susceptibility maps depend on the observations of landslides considered: all types of landslides,
debris avalanches only, or source areas of debris avalanches. These observational datasets
reflect the detection of different landslide processes or components, which relate to different
landslide-inducing factors. For each landslide dataset, a Stability Index (SI) is calculated as a
multiplicative result of the frequency ratios for all attributes and is mapped across our study
domain in the North Cascades National Park Complex, Washington, U.S.A. A continuous

1 function is developed to relate local SI values to landslide probability based on a ratio of
2 landslide and non-landslide grid cells. The empirical model probability derived from the debris
3 avalanche source area dataset is combined probabilistically with a previously developed
4 physically-based probabilistic model. A two-dimensional binning method employs empirical
5 and physically-based probabilities as indices and calculates a joint probability of landsliding at
6 the intersections of probability bins. A ratio of the joint probability and the physically-based
7 model bin probability is used as a weight to adjust the original physically-based probability at
8 each grid cell given empirical evidence. The resulting integrated probability of landslide
9 initiation hazard includes mechanisms not captured by the infinite slope stability model alone.
10 Improvements in distinguishing potentially unstable areas with the proposed integrated model
11 are statistically quantified. We provide multiple landslide hazard maps that land managers can
12 use for planning and decision making, as well as for educating the public about hazards from
13 landslides in this remote high-relief terrain.

1 Introduction

15 Most mountain ranges are susceptible to landsliding due to their steep geomorphology, loose soil
16 development, geology, and high precipitation (e.g., Coe, 2016). Landslides disrupt aquatic
17 habitats (May et al., 2009; Pollock, 1998), damage infrastructure such as roads, utilities, and
18 dams (Ghirotti, 2012; Baum et al., 2008), and harm people (Wartman et al., 2016; Taylor and
19 Brabb, 1986). Landslide hazards are expected to increase globally with growing extremes in the
20 climate (Coe, 2016; Haeberli et al., 2016; Crozier 2010).
21
22 Maps of landslide hazards, quantified as a probability of landslide initiation or impact, can be
23 obtained using empirical methods that statistically relate the location of existing landslides to
24 other environmental variables and physically-based models based on geotechnical slope stability
25 equations driven by hydro-climatic inputs (Bordoni et al., 2015; Mancini et al., 2010; Sidle and
26 Ochiai 2006; El-Ramly, et al., 2002). While detailed quantitative and categorical climatic,
27 geologic, ecologic, and pedologic information can be used in statistical models, physically-based
28 models are limited to geotechnical stability analysis driven by soil pore-water pressure, and often
29 neglect geological factors such as bedrock, faulting, and complexities of microclimatic
30 conditions. To date, data-driven empirical research on landslide hazard mapping (Corominas et
31 al., 2012; Lee 2007; Chung and Fabbri 2002) has been typically conducted independently from
32 hydroclimate-driven modeling of landslides that largely focus on hydrologic controls on
33 landsliding (Wooten et al., 2016; Cevasco et al., 2014). There is need for unifying these two lines
34 of research to provide regional scale landslide prediction for resource management and hazard
35 mitigation strategies. In this paper we develop a statistical approach to combine probability of
36 landslide initiation obtained from an observation-based statistical mapping method and a
37 physically-based model. The proposed approach is illustrated in the North Cascades region of
38 the state of Washington, USA.
39
40 Data-driven statistical landslide susceptibility approaches assess the inherent or quasi-static
41 stability of hillslopes derived from statistical associations (e.g., correlations) between site
42 attributes (e.g., soil, geology, topography) and an inventory of past landslides that includes
43 landslide type and locations (e.g., Dai and Lee, 2002; Gupta and Joshi, 1990; Pachauri and Pant,
44 1992; Kirschbaum et al., 2012). These models focus on prevailing conditions that predispose

hillslopes to failure (Hungr et al., 2014), typically providing general indices of relative landslide susceptibility or spatial probabilities applicable to the study location and cannot represent causal factors or triggering conditions that change in time (van Westen et al., 2006; Sidle and Ochiai, 2006). Outcome of such analyses depend on the completeness of observations, hindering the use of such techniques over large areas where complete inventories are typically lacking. Since empirical models are based on observation of past landslides, the preconditioning relationships are assumed to prevail into the future until an updated study is completed (Lepore et al., 2012).

Physically-based models require considerable data on the spatial-temporal characteristics of the landscape and triggering hydro-meteorologic events. These models are also usually restricted to a specific type of landslide and can be limited in representing local geologic, soil, and hydrologic conditions that may be difficult to observe and map in the field and parameterize in model theory. Data-driven statistical methods could be used to condition physically-based model results to incorporate the influence of environmental and geologic factors that are not represented in process theory. Linking these empirically-based and physically-based models may improve the spatial-temporal patterns of landslide hazard at medium to large scales where landslide inventories exist to provide support tools for authorities addressing risk management Additional descriptions of the advantages and disadvantages of data-driven and physically-based models and landslide hazards assessments can be found in reviews by Ercanoglu and Sonmez (2019), Reichenback, et al. (2018), Hungr (2018), and Aleotti and Chowdhury (1999).

This paper describes research designed to address the following questions: 1) How can we quantify relative contributions of local topography, geology, and ecology on landslide frequency and derive spatial probabilities of landsliding using a statistical model? 2) How would probabilities of landslide initiation derived from empirical observations compare with those derived from a physically-based model? 3) How can we combine empirical and physically-based models for landslide susceptibility to improve the prediction of landslide hazards?

The empirical approach for landslide susceptibility we used is based on a modification of the Frequency Ratio (FR) statistical concept which has been found to perform as well as more rigorous statistical approaches such as logistic regression (Hong et al., 2017; Wu et al., 2017; Bellugi et al., 2015; Lepore et al., 2012; Kirschbaum et al., 2012; Lee and Pradhan, 2007; Lee et al., 2007). As for the mechanistic model, we used the results of Strauch et al. (2018), who developed a Monte Carlo solution of the infinite slope stability equation coupled to a steady-state topographic flow routing approach to map annual probability of shallow landsliding. The uncertainty of soil depth in Strauch et al. (2018) was constrained by a soil development model, and subsurface flow recharge was obtained from a regional macro-scale hydrologic model that produced historical hydrologic simulations (Hamlet et al., 2013).

Building on the advantages from the empirical and process models, we combined the two models to develop a map of landslide hazard. The integrated map can be developed to identify landslide hazards that may originate from the initiation of landslides and used to inform models of transport and deposition (i.e., runout) of landslide material (Fig. 1). The focus of the study was to determine if an empirical-based model of landslide hazard could be used to improve an existing physically-based model for shallow landslide probability. The organization of this paper

is as follows. Our methodology is discussed in Sect. 2, including the empirical method, model application, data compilation, and model integration approach. Sect. 3 details our results of the empirical application and integrated hazard model as well as various hazard maps developed. We end with some overall concluding thoughts in Sect. 4.
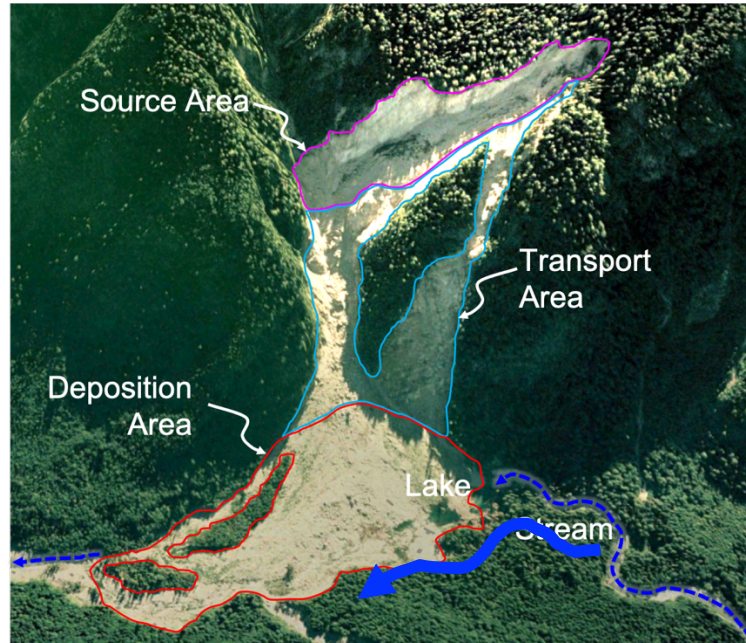
Figure 1. Primary landslide features of the Goodell Creek landslide (Oct. 2003) showing source, transport, and deposition areas illustrated over aerial image from Google Earth. Base of landslide is about 1 km across. Location in North Cascades National Park Complex about 4 km north of Newhalem, Washington. Source: Google Earth, 48°41'55.72" N 121°17'01.31" W, imagery data June 23, 2006 viewed towards southwest.

2 Methodology

2.1 Frequency Ratio

We characterized the susceptibility of hillslopes to landslides using an empirically-based Frequency Ratio, FR, approach (Lee et al., 2007; Kirschbaum et al., 2012). We used the term landslides broadly, covering all types of mapped landslides in our landslide inventory, with their source, transport and depositional zones (Fig. 1). The FR approach relates the density ratio of historical landslides within selected surface attributes, SAs. We considered seven SAs in our analysis: slope, elevation, aspect, curvature, land use-land cover (landcover), lithology, and topographic wetness index.

Slope, curvature, and lithology directly affect the forces and geotechnical properties in surface sediments. Land cover provides a surrogate for root cohesion and topographic wetness index has been used as a surrogate for soil pore water pressure (Borga et al., 2002). Elevation can represent the effects of climate, weathering, vegetation, ground motion, and glacial processes, if any, as well as coincide with variability in slope, soil depth, and land use (Sidle and Ochiai,

4

1 2006). Aspect provides an indication of solar insolation, vegetation type and cover density, snow
2 and ice loading, and soil moisture levels via evapotranspiration (Beaty, 1956; Gokceoglu et al.,
3 2005).

4 Each SA is indexed by attribute type, m (e.g. m=slope, lithology, vegetation), and its subcategory
5 is indexed by n. Subcategories of each SA can be a categorical variable such as type of lithology,
6 soil and vegetation, or a quantitative variable defined with certain ranges such as slope and
7 aspect over the study domain, SD. For a given SA, identified by m, and its subcategory, n,
8 $FR_{m,n}|SA_{m,n}$ is calculated (Eq. 1) as the ratio of observed landslide area, LA, in each SA m and
9 subcategory n ($LA_{SAm,n}$) with respect to the area of the $SA_{m,n}$ ($A_{SAm,n}$) to the regional landslide
10 density, P_o (Eq. 2) (Miller and Burnett, 2007):

11 $$FR_{m,n}|SA_{m,n} = \frac{LA_{SAm,n}/A_{SAm,n}}{P_o}$$ (1)

12 where $P_o = \frac{LA_{SD}}{A_{SD}}$ (2)

13 The term in the numerator of Eq. (1) gives an empirical probability of landsliding impact within
14 $SA_{m,n}$. *Po* can also be referred to as a regional background probability, such that in absence of
15 any other information, *Po* represents the probability of landsliding at any point in the domain.
16 The interpretation of FR is as follows (Lepore et al., 2012):
17   ● FR < 1: indicates proportionally less landslide area with subcategory n of SA m, $SA_{m,n}$;
18   hence, smaller odds of a landslide than in the entire SD.
19   ● FR = 1: means there is the same proportion of landslide area with $SA_{m,n}$ as in the SD thus,
20   the odds of a landslide are the same for the $SA_{m,n}$ subcategory as the SD.
21   ● FR > 1: reveals a higher percentage of landslide area with $SA_{m,n}$, than in the entire SD,
22   so there is a propensity for failures to occur with this SA.
23
24 FR in Eq. (1) is developed for a population of spatially distributed locations that has the same
25 attribute of a given $SA_{m,n}$. A given point on the landscape would have as many FR values as the
26 number of SAs used. To develop an index that will incorporate all the FR values for a given
27 point on the landscape we used an empirical susceptibility index, SI, defined at the grid cell
28 scale, SI_c, as the product of the FR values for all SAs of that grid cell and their associated
29 subcategory,
30
31 $$SI_c = \prod^m FR_{m,n}|SA_{m,n}.$$ (3)
32
33 A multiplicative FR is used because in certain subcategories, there may be no landslide
34 observations (e.g., low slope angle), and in such cases the hillslope would be stable regardless of
35 other soil and vegetation properties. SI_c is a measure that relates local static (or slowly changing)
36 site characteristics to relative frequency of landslides. Since SI_c is a data-driven index,
37 probability of landsliding would increase as SI grows.
38
39 In order to develop a continuous relationship between SI_c and probability of landslide at a grid
40 cell, $P(LS_c|SI_c)$, we binned the population of SI_c values across the landscape into SI_r bins, where r

is the number of SI bins. We then estimated the probability of landsliding for an SI bin, SI_r, $P(LS_r|SI_r)$, as the ratio of number of grid cells with landslides in each SI bin, $N(LS)_r$, to the total number of grid cells within each SI bin, N_r (Eq. 4).

$$P(LS_r|SI_r) = \frac{N(LS)_r}{N_r}$$
(4)

To calculate spatially continuous empirical probability of landsliding at each grid cell of a DEM, $P(LS_c|SI_c)$, we fit empirical functions that relate $P(LS_r|SI_r)$ to SI_r. These functions are then used for mapping empirical probability of landsliding at the cell scale, $P(LS_c|SI_c)$, based on its empirically-derived SI_c value in Eq. (3).

We included all SAs to develop empirical models relating SI to landslide probability, similar to Kirschbaum et al. (2012) and Lepore et al. (2012). We repeated the analysis described above three times: first, considering all landslide types and including their source, transport, and depositional zones, as is commonly done in multi-factor analyses (Sidle and Ochiai, 2006; Ayalew et al., 2004; Carrara et al., 1995); second, focusing on debris avalanches, with all three of their zones (Fig. 1); and third, considering only the source (initiation) areas of debris avalanches. These source areas were identified as the upper 20% by elevation within mapped debris avalanche polygons, which appeared to align with inspections of aerial imagery of a selected debris avalanches. This tiered approach can be used to quantify the relative contributions of different landslide features to overall landslide hazard in a region as well as inform the variability in hazard identification given a landslide dataset.

2.2 Model Integration

Here we develop a method to combine the empirical probability for landslide initiation based on SI, $P(LS_c|SI_c)$, with the probability of landslide initiation based on a previously developed physically-based model using Landlab (Strauch et al., 2018; Hobley et al., 2017). The physically-based model employs Monte Carlo solution of the infinite slope stability model that evaluates localized (model grid cell) factor of safety (FS), and calculates the annual probability of failure at a cell, $P(FS_c \leq 1)$ as the number of Monte Carlo iterations where probability of failure ≤ 1 divided by the total number of iterations. Precipitation is considered in the physically-based model through its use as input to a macro-scale hydrology model, such as the Variable Infiltration Capacity model (Liang et al. 1994), which produces a spatially distributed recharge field used to drive the steady-state subsurface flow model in the component. Other hydro-geophysical stochastic inputs into the stability model are selected from distributions while slope and specific contributing area are deterministic variables.

In combining probabilities, we focus on the landslide *initiation* areas, as the physically-based model we used would only be applicable for landslide initiation. Empirical $P(LS_c|SI_c)$ and modeled $P(FS_c \leq 1)$ probabilities of landslide impact at each cell defined across the landscape are treated as indices representing the likelihood of landslides. The method we proposed for an integrated probability uses the cell count of observed landslide initiation points within bins of the empirical, $P(LS_c|SI_c)_b$, and modeled probability, $P(FS_c \leq 1)_b$ of landsliding.

1　If we treat the empirical probability as an index, the probability of landslide initiation within a
2　bin *j* of empirically-derived probability of landslide initiation, $E_j = P(LS_c|SI_c)_{b,j}$ is calculated as:

3　$$P(LS|E_j) = \frac{N(LS)_j}{N_j} \qquad\qquad (5)$$

4　where, $N(LS)_j$ is the number grid cells with observed landslides and N_j is the number of grid
5　cells both in bin j of E_j:
6
7　Similarly, the probability of landslide initiation within a bin *i* of physically-based modeled
8　probability of landslide initiation, $M_i = P(FS_c \le 1)_{b,i}$ is calculated as:

9　$$P(LS|M_i) = \frac{N(LS)_i}{N_i} \qquad\qquad (6)$$

10　where, $N(LS)_i$ is the number of grid cells with observed landslides and N_i is the number of grid
11　cells both in bin i of M_i. If the observed landslide data is representative of the actual landslide
12　frequency over the duration when the probability of landsliding is modeled, an ideal model that
13　correctly represents all environmental variables associated with landslide initiation would give
14　$P(LS|M_i) = M_i$. Assuming unbiased landslide mapping in the field, a greater difference
15　between these two relative frequency probabilities would suggest a weaker model representation
16　of the process, especially when the physically-based model is run to represent landslide risk for a
17　given climatology.
18
19　Modeled probabilities may be improved when information contained in empirical probabilities is
20　introduced. The probability of landslide initiation in areas shared by any two select bins (e.g., co-
21　bins) of empirically-derived, E_j, and physically-based modeled, M_j, probabilities is calculated as
22　the joint probability:

23　$$P(LS|E_j \cap M_i) = \frac{N(LS)_{j,i}}{N_{j,i}} \qquad\qquad (7)$$

24　where $N(LS)_{j,i}$ is the number grid cells with observed landslides and $N_{j,i}$ is the number of grid
25　cells in the *joint* bin j of empirical probability and bin i of modeled probability data. An
26　illustration of this estimation is given in Figure 2. The conceptual example shows how relatively
27　low landslide probability predictions by a process model in the M_i=0-0.2 bin range can be
28　modified due to differences in the empirical preconditioning of the landscape (e.g., rock type) to
29　landslides represented in E_j. The intersection of M_i=0-0.2 with E_j=0.2-0.3 yields a higher
30　empirical probability of landsliding. Influence of vegetation change and extreme weather events
31　(e.g. Eco-hydrometeorologic controls) that were not part of the initial empirical data set used for
32　estimating E_j bins can be captured by the physically-based model. In this case the model predicts
33　a high probability M_j=0.8-1, while E_i remained in the low probability range in E_i=0.0-0.1. The
34　intersection of M_j and E_i land surface characterization captures the landscape where landslides
35　were observed.
36
37
38

7
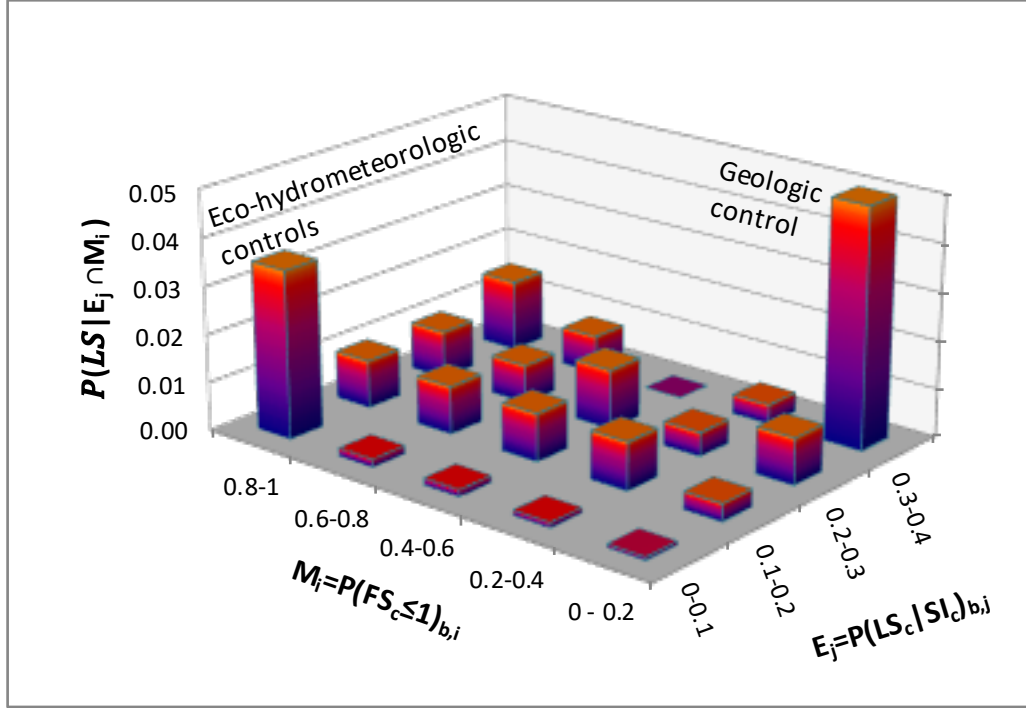
Figure 2. Illustration of the proposed landslide probability conditioned on estimated spatially distributed SI-based empirical and modeled probabilities as binned indices, E_J and M_i, that form a joint space. $P(LS|E_j \cap M_i)$ is defined as the ratio of the number of landsliding cells to the number of cells that jointly fall into given E_J and M_i bins.

We propose that the ratio of $P(LS|E_j \cap M_i)$ and $P(LS|M_i)$ can be used as a correction to $P(FS_c \leq 1)$. As model predictions improve, this ratio should get closer to 1, especially when the model is used to map landslide probability for a given climatology in a region. When the physically-based model is run for studying a specific rainfall event, this ratio quantifies the relative roles of other factors could play on landslide initiation. Thus, we propose that the probability of landsliding at each grid cell, c, given the corresponding M_j and E_i bins that a cell belongs to can be estimated as:

$$P(LS)_{c,j,i} = P(FS_c \leq 1) \times \frac{P(LS|E_j \cap M_i)}{P(LS|M_i)} \qquad (8)$$

If we let ω represent the bin-based ratio on the right-hand side of Eq. (8) as a weighting factor based on observations of landslides, then we can simplify notation to:

$$P(LS)_{c,j,i} = P(FS_c \leq 1) \times \omega \qquad (9)$$

This gives the probability of landslide initiation, represented as an *adjusted* modeled probability of landslide initiation at a grid cell given empirical observations correlated with site characteristics. In the reminder of the paper we use $P(FS_c \leq 1)$ to refer to physically-based

1 shallow landslide probability from Strauch et al., (2018) and P(LS) to refer to the adjusted model
2 probability using the proposed empirical-adjustment methodology.

3 A hypothetical example shown in Table 1 demonstrates calculating the relative frequencies, the
4 resulting calculated weight, and adjusted P(LS) (Eq. 9). The calculation of relative frequency is
5 based on binning modeled and empirical probabilities, counting landslide and non-landslide cells
6 within each bin, and calculating a weighting term, ω, which is then used to adjust the original
7 modeled probability given empirical evidence. Weights can be greater than 1 and the final
8 probability will be increased when weight $\geq$ 1 and decreased when weight < 1. Final adjusted
9 probabilities are limited to unity in the integrated model. For example, a weight = 2 and modeled
10 probability = 0.2 would result in a doubling of the final probability = 0.4 given empirical
11 information.

12 **Table 1.** Hypothetical example of calculating relative frequencies, weight, and P(LS) during
13 model integration

E_j bins	Observed Landslides / Total Cell Count *(relative frequency)*					Total
0.2-0.3	206/ 870	5/ 24	3/ 14	5/ 14	2/ 10	221/ 932
0.1-0.2	11107/ 87104	309/ 2001	193/ 1220	137/ 856	96/ 657	11842/ 91838
0 – 0.1	48513/ 1848950	**1757/ 51679**	1157/ 33084	793/ 24928	742/ 21410	**52962/ 1980051**
Total	59826/ 1936924	**2071/ 53704**	1353/ 34318	935/ 25798	840/ 22077	65025/ 2072821
M_i bins	*0-0.1*	*0.1-0.2*	*0.2-0.3*	*0.3-0.4*	*0.4-0.5*	

An example calculation of P(LS) using the above data − a cell having a modeled probability, $P(FS_c \leq 1) = 0.12$ and an empirical probability, $P(LS_c|SI_c) = 0.08$, then:
$P(LS|E_j) = 52962/1980051 = 0.027$ (Eq. 5)
$P(LS|M_i) = 2071/53704 = 0.039$ (Eq. 6)
$P(LS|E_j \cap M_i) = 1757/51679 = 0.034$ (Eq. 7)
$\omega = 0.034/0.039 = 0.87$
$P(LS)_{c,i,j} = 0.12 \times 0.87 = 0.105$ (Eq. 9)

14

15 2.3 Model application
16 2.3.1 Study Area
17 Our study area is within the geographical limits of North Cascades National Park Complex
18 (NOCA) managed by the U.S. National Park Service (Fig. 3). NOCA has experienced damaging
19 and disruptive landslides that have impacted infrastructure and disrupted public use of the park.
20 NOCA is approximately 2,757 km^2, with 93% wilderness (e.g., no motorized or mechanized
21 devices) (DOI-NPS, 2012), which is ideal for studying landslides primarily triggered by natural
22 causes. The north-south oriented Cascade Mountains has an elevation range of 100 to 2,800 m at
23 the study site, with jagged bedrock peaks, and over 300 alpine glaciers. The landscape has been
24 shaped by Ice Age continental and alpine glaciers, and mass wasting, fluvial and tectonic uplift
25 processes that continue today (LaHusen et al., 2016; Mustoe and Leopold, 2014; Collins and
26 Montgomery, 2001; Riedel et al., 2007; Pelto and Riedel, 2001). The bedrock geology in the
27 park is dominated by gneiss and granite, with lower grade metamorphic rocks schist and phyllite

1 on the western edge of the park, and Mesozoic sedimentary rocks on the eastern flank (Tabor and
2 Haugerud, 1999). Placement of granite at depth along faults led to hydrothermal alteration of
3 some overlying rocks, and the clustering of large landslides. Soils in the park are generally
4 coarse-grained and relatively young due to active slope processes, but soil age, thickness and
5 distribution are highly variable. Soils formed in glacial deposits from the last glaciation are also
6 widespread, and many soils are classified based on the amount of volcanic ash they contain.
7
8 Orographic uplift of Pacific Ocean air masses generates a spatial precipitation gradient with an
9 average of 4,575 mm of precipitation falling annually on the highest elevations west of the crest,
10 while lowlands east of the crest receive a mean annual precipitation of 708 mm (Mustoe and
11 Leopold, 2014; Roe, 2005). Air temperatures vary highly depending on season and elevation
12 with the warmest month typically August and the coldest month is January; corresponding
13 average daily temperatures of about 25° C and 4°C, respectively, for these months in Newhalem,
14 Washington.
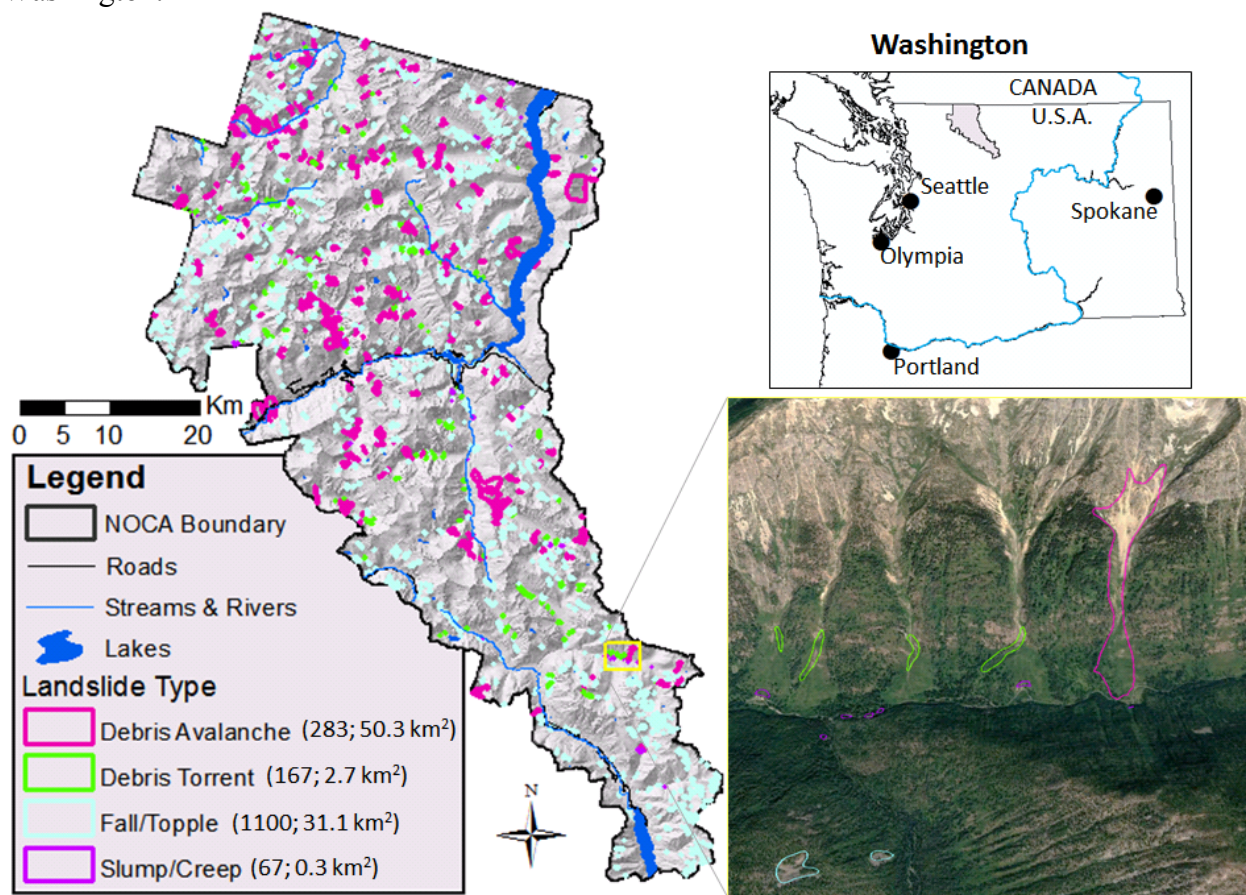
15
16
17 **Figure 3.** Four landslide types mapped within North Cascades National Park Complex (NOCA) in
18 Washington, U.S.A. The number and their total area of each type is given in parentheses. Insert provides
19 example of mapping over aerial image from Google Earth, 48°27'20.21" N 120°44'47.09" W, imagery data
20 August 27, 2006.
21
22 Vegetation in NOCA is dominated by forest, particularly coniferous tree species, up to about
23 2,000 m (Strauch et al., 2018; Agee and Kertis, 1987). A patchwork of shrubs, herbaceous

10

vegetation, and barren land is found above this elevation common in alpine environments and in the paths of frequent snow avalanches. Above 2,400 m is mostly bare rock, snow and ice. The underlying geology is composed of a primarily old Mesozoic crystalline and metamorphic rock originating far to the south (Haugerud and Tabor, 2009).

Landslide (LS) inventory data are the most requisite information needed for an empirical statistical analysis (Lepore et al., 2012). Landslides were mapped in the 2,768 km^2 park as discreet landforms during a comprehensive park-wide landslide inventory (Fig. 3; Riedel and Probala, 2005). Landslides were identified using stereo-pair air photos taken since the 1960s at 1:24,000 and 1:12,000 scales, 7.5 minute topographic maps, bedrock geology maps, and field investigations (e.g., Riedel et al., 2012). The minimum mapping unit was approximately 1,000 m^2 except for some smaller slump units. Landslide linework was transferred to a digital format, peer reviewed, and polygons edited into final form in geographical information system (GIS) software using National Agriculture Imagery Program (NAIP) imagery and a 10-m DEM and, in some cases, LiDAR. Where areas were mapped by traditional methods, and LiDAR later became available, the original approach captured most (~75%) of the landslides. Dense vegetation cover and a lack of access limited identification of some existing landslides. Larger, more recent debris avalanches that left large deposits on the valley floor were more easily recognized and mapped. Ancient landslides that occurred before the last glacial period 16,000 years ago were generally not mapped because their deposits were buried or reworked by subsequent continental glaciation.

The landform mapping study identified six different types of mass wasting: rock fall/topple, debris avalanche, debris torrent, slump/creep, sackung, and snow avalanche-impacted landforms (SAILs) of which four are described in Table 2 (Riedel et al., 2012). The single sackung mapped in NOCA represents a gravitational spreading or slope deformation, sometimes found near ridge tops. All landslide types were included in the analysis except for the rare sackung and SAILs, which are created by snow avalanche impacting unconsolidated sediments rather than slope instability. The idea is to capture more spatial variability and geologic controls on observed landslides by using all the data we obtained for available from the inventory for the four common landslide types. There are 1,618 landslides mapped in NOCA: falls/topples (68%), debris avalanches (17%), debris torrents (10%), slumps/creeps (4%), and one sackung (<1%) (Fig. 3; sackung not shown).

Table 2. Landslides mapped as part of comprehensive landform mapping study used in hazard analysis (Riedel et al., 2005)

Type of Mass Wasting	Process	Mapping
Debris Avalanche	Extremely rapid moving mixture of rock, soil, and vegetation, generally originates from glacially-sourced areas, over-steepened valley walls, and in many cases hydrothermally altered bedrock	Includes headwall scar, path, and deposit

Debris Torrent	Channelized rapid and/or sudden flow of material entraining debris stored in stream channel while moving down slope	Only the deposition areas within a debris cone
Slump and Creep	Slumps - rotational slip of cohesive sediments, usually triggered by undercutting of steep slopes along riverbanks. Creeps - slow movement induced by saturated ground.	Mapped where deciduous vegetation brighter on aerial photos, fresh new soil, jackstraw or pistol gripped trees.
Rockfall or Rock Topple	Sporadic and shallow detachment of rock falling from bedrock cliffs and rock towers	Mapped where bright and highly reflective with little or no vegetation on aerial photos. Mainly deposition mapped.

1
2   2.3.2 Study domain and Parameters
3   We constrained our analysis to soil-mantled landscapes by excluding high elevation areas
4   covered by glaciers, permanent snowfields and exposed bedrock, as well as wetlands and other
5   water surfaces, based on landform mapping and maps of lithology and landcover. We also
6   exclude slopes less than 17° because this slope threshold was found to generally separate
7   colluvial mass wasting and debris transport processes from fluvial processes in this region
8   (Strauch et al., 2018). The area included in the analysis covers about 79% of NOCA's land area.
9
10 The seven site attributes (SAs) investigated using the Frequency Ratio (FR) approach as they
11 relate to mapped landslide activity vary across the NOCA study area. Slope, total curvature
12 (Laplacian of elevation), and aspect attributes were derived using ArcGIS from a 30-m digital
13 elevation model (DEM) acquired from National Elevation Dataset (NED) (USGS, 2014a). A
14 resolution of 30-m was chosen for comparability with other studies and landslide size (e.g.,
15 Strauch et al., 2018; Lepore et al., 2012). Elevation ranges from 107 to 2794 m with 85% of the
16 park between 500 to 2000 m. Subcategories for elevation were based on 200-m increments with
17 lumping at the ends (e.g., < 400 m and > 2200 m). Slope subcategories were set at 5° increments
18 with ending subcategories for slopes 17-25°, and >50°. Curvature was divided into three
19 subcategories: convex/diverging, flat, or concave/converging. Aspect (i.e., facing direction of
20 slope) was classified into eight compass orientations (i.e., N, NE, E, SE, S, SW, W, NW). The
21 park's complex topography results in roughly equal distribution among the cardinal and
22 intercardinal directions of aspect; however, the southwest quadrant is slightly more common.
23
24 The DEM also provides the information needed to derive a distributed wetness index (Beven and
25 Kirkby, 1979; O'Loughlin, 1986), calculated as the natural log of the ratio of specific catchment
26 area [L] to sine of local slope. This index has been used for quantifying the contribution of pore-
27 water pressure to destabilizing forces in landslide modeling (e.g., Borga et al., 2002; Gokceoglu
28 et al., 2005). Wetness index was divided into 5 subcategories based on 20% quantiles: low, low-
29 medium, medium, medium-high, and high wetness. Landcover was acquired from the 2014
30 National Land Cover Data (NLCD), which is based on 2011 Landsat satellite imagery (Jin et al.,

2013; USGS, 2014b). We categorized this into forest, shrubland, herbaceous, water, wetland, snow/ice, barren, and developed (e.g., roads, campgrounds). Based on this classification, forest, shrubs, and herbaceous vegetation represent 54%, 15%, and 10% of the park, respectively. Barren and snow or ice combined cover 17%, typically at the high elevations. Water and wetlands cover about 2.5%, while developed is less than 0.5%.

Lithology provides a description of rock and deposits that indicates composition, strength, and age, which can influence the hillslope strength and water redistribution. Washington State Department of Natural Resources (WADNR) provides lithology in its surface geology maps that display rocks and deposits as geologic map units (WADNR, 2014). This source of information was chosen because it is available for all of Washington, facilitating future applications. There are 48 lithology map unit types within NOCA. These were aggregated into seven subcategories, based on similarities in origin and generally increasing strength, called: (1) unconsolidated sediment, (2) ultramafic, (3) weak metamorphic foliated, (4) sedimentary rock, (5) hard metamorphic, (6) intrusive igneous, and (7) volcanic/extrusive igneous (Table 3). Water and ice were not classified. Both landcover and lithology were rasterized to the same DEM grid resolution using ArcGIS based on the dominant type of attribute in each grid cell. Among the seven types of lithology, hard metamorphic is most common (41% of NOCA), while ultramafic, sedimentary rock, and volcanic/extrusive igneous combined make up less than 5%.

Table 3. Classification of Washington Department of Natural Resources surface geology from generally weaker (1) to stronger (7) material along with aerial percentages within NOCA in parentheses

| Class	WADNR Lithology	Class	WADNR Lithology
Unconsolidated Sediments (12%)		**Sedimentary Rock** (2%)	
1	alluvial fan deposits	4	sedimentary deposits or rocks, undivided
	alluvium		continental sedimentary deposits or rocks
	alluvium, older (e.g., alluvial fans & talus)		marine metasedimentary rocks
	alpine glacial drift, Fraser-age		marine sedimentary rocks
	alpine glacial till, Fraser-age	**Hard Metamorphic** (41%)	
	glacial outwash, alpine, Fraser-age	5	banded gneiss
	continental glacial drift, Fraser-age		mixed metamorphic and igneous rocks
	mass-wasting deposits		orthogneiss
	mass-wasting deposits, mostly landslides		paragneiss
	mass-wasting deposits, not landslides	**Intrusive Igneous** (21%)	
	peat deposits	6	acidic (felsic) intrusive rock
	talus deposits		basic (mafic) intrusive rocks
Ultramafic (0.02%)			diorite
2	ultrabasic (ultramafic) rocks (*serpentine*)		gabbro
Weak Metamorphic Foliated (14%)			granite
3	heterogeneous metamorphic rocks		granodiorite
	hetero. metamorphic rocks, chert bearing		Intermediate intrusive rocks
	marble		Intrusive breccia

	metasedimentary and metavolcanic rocks		quartz diorite
	metasedimentary rocks		quartz monzonite
	metasedimentary rocks, cherty		tonalite
	metavolcanic rocks	**Volcanic/Extrusive Igneous** (2%)	
	amphibolite		tuffs and tuff breccias
	phyllite, low grade	7	dacite flows
	schist, low grade		rhyolite flows
--	Water and Ice (7%)		volcanic breccia

3 Results and Discussion

3.1 Frequency Ratio Analysis

The results of the FR analyses for each site attribute (SA) are presented in Fig. 4. We discuss the role of SA starting with debris avalanche source areas as they are hypothesized to represent the initiation processes of shallow landslides that transform into debris avalanches. The SAs that impact shallow landslide initiation could arguably play common controls on the initiation of other types of slope failures. The frequency analysis shows a clear and growing control of local slopes greater than 35º on landslide initiation, which can be considered as the internal friction angle of cohesionless sand (Fig. 4c).
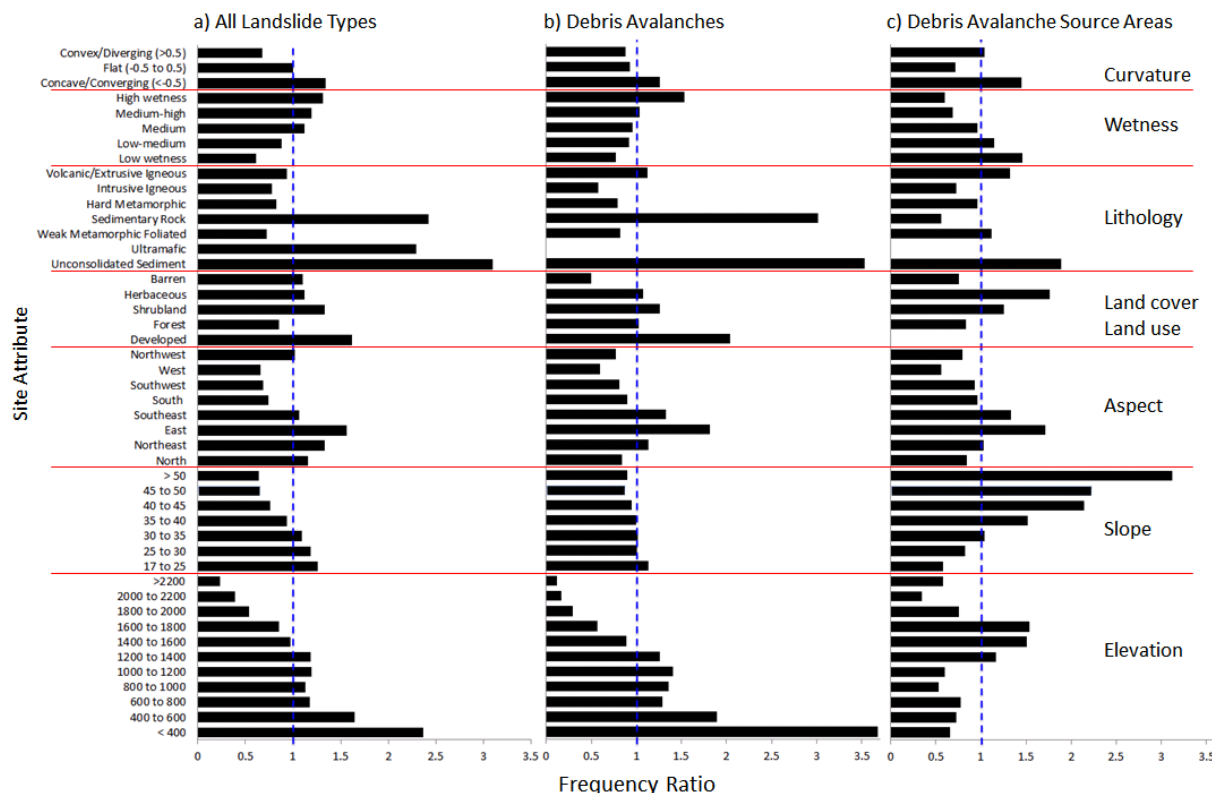
Figure 4. FR value for different bins of seven Site Attributes (SA) separated by red lines, based on **(a)** all landslide types mapped within the NOCA study domain, **(b)** debris avalanche landslide types only, and **(c)** source areas of debris avalanches represented by the highest 20% of the mapped debris avalanche.

1   The vertical blue line refers to the FR value of 1.0, denoting when no association is found with mapped
2   landslides. FR values below this line are attributes less likely associated with landslides and FR values
3   above this line indicate greater association with landslides.
4
5   The source area of debris avalanches is only about 17% of the mapped debris avalanche area and
6   10% of the whole landslide inventory, which predominantly maps transport and depositional
7   areas. A small debris avalanche source area in steep terrain can lead to large landslide impacts in
8   lower elevations, as the eroded material travels downhill and deposits in gentler gradients (Fig.
9   1). Thus, the runout zones of debris avalanches and other mapped landslide types cover more
10 area at gentler slopes typical of lower elevations. This process is captured in Fig. 4a and 4b
11 where the FR analyses exhibit higher landslide hazard at gentler slopes (<30º), more likely
12 associated with transport and depositional processes as well as failure of side slopes along
13 glacially incised U-shaped valleys undercut by fluvial activity. Others have reported clustering of
14 landslide impacts in lower elevations within valleys where hillslopes are steep enough to fail
15 (Megahan et al., 1978; Kelsey, 1988; Densmore et al., 1997; Chalkias et al., 2014).
16
17 In the study area, local slopes generally increase on average with elevation, particularly above
18 1,400 m (Strauch et al., 2018). The control of steeper slopes on debris avalanche initiation is
19 supported by the results for elevation where source areas are associated with mid to high
20 elevation (1,400 to 1,800 m) and entire debris avalanches and all landslides types, including
21 deposition zones, have growing frequency in lower elevations (< 1,200 m) with the highest
22 frequency falling in elevations <400 m (Fig. 4a, b). Further increase in slopes typically lead to
23 bedrock exposure and barren lands with thin soil (Strauch et al., 2018; Gabet, 2003). In addition
24 to steepening slopes, the observed higher frequency of debris avalanche source areas in the mid-
25 to-high elevation range corroborates recent findings of an ecosystem transition control on
26 landslide initiation (Strauch et al., 2018). With the cooling of air temperatures beyond forest
27 ecosystem thresholds, the transition of forest vegetation (predominant alpine conifers) to mixed
28 shrub and herbaceous vegetation types with lower root cohesion, lead to higher landslide
29 frequency at debris avalanche source areas (Fig 4c). The slope and elevation results, however,
30 are likely influenced by the mapping approach, which was biased in mapping landslide activity
31 on the lower portions of hillslopes that were typically more accessible, and continuous creep and
32 rapid slides in subalpine and alpine areas were infrequently mapped.
33
34 Developed areas that include impervious surfaces, constructed materials, and lawns have the
35 highest landcover association with all mapped landslide areas, as well as with debris avalanches,
36 yet no association with debris avalanche source areas, which are typically higher on mountains
37 and rarely developed. Although dirt roads have been found to disrupt drainage and increase
38 erosion (Croke and Hairsine, 2006; Montgomery, 1994; Swanson and Dyrness, 1975), the lack of
39 association with landslide initiation suggest that these areas may be positioned on the landscape
40 in areas likely to be impacted by landslide runout or deposition. In general, forest and barren
41 landcover show the least landslide activity compared to other landcover (Fig. 4). The forest
42 association likely indicates the positive contribution of root cohesion to hillslope stability,
43 whereas the barren landcover type results may indicate the effect of mapping completeness or
44 hillslope processes. The barren results appear counter to the findings of the physically-based
45 landslide model applied at the same location, which found high probability of landslide initiation
46 in barren areas often below retreating glaciers (Strauch et al., 2018). Barren includes areas of

1 bedrock, glacial debris, and other accumulations of earthen material with vegetation generally
2 accounting for less than 15% of total cover; thus, there may be a variety of stability conditions
3 within this single cover class.
4
5 The sources of debris avalanches are linked to eastern and southeastern aspects (Fig. 4c); 20%
6 and 15% of source cells by area occur on these aspects, respectively. Except for western aspects
7 that show the weakest association debris avalanches, other aspects show landsliding frequency
8 close to the average frequency in the whole study domain. Vegetation type and cover that relate
9 to root strength and moisture regime can be related to aspect. East and south exposures have
10 lower forest cover fractions compared to other aspects at mid to lower elevations (< 1,400 m),
11 and forests are largely replaced by barren lands and shrub and herbaceous vegetation as elevation
12 increases (Fig. 5). Most source areas of debris avalanches and debris avalanches as a whole are
13 associated with shrub and herbaceous vegetation types (Fig. 4b,c). Other aspects, especially
14 west-facing slopes have higher fraction of forest cover (Fig. 5), likely linked to a longer growing
15 season (Evans and Fonda 1990). Lower landslide frequency in western aspects can be a result of
16 higher root cohesion of forest vegetation compared to shrub and herbs. Additionally, perhaps
17 west-facing aspects experience more arid moisture regimes or bedrock bedding, jointing, or
18 fracturing conducive to stability compared to other exposures (Carson and Kirby, 1972; Fischer
19 et al., 2006).
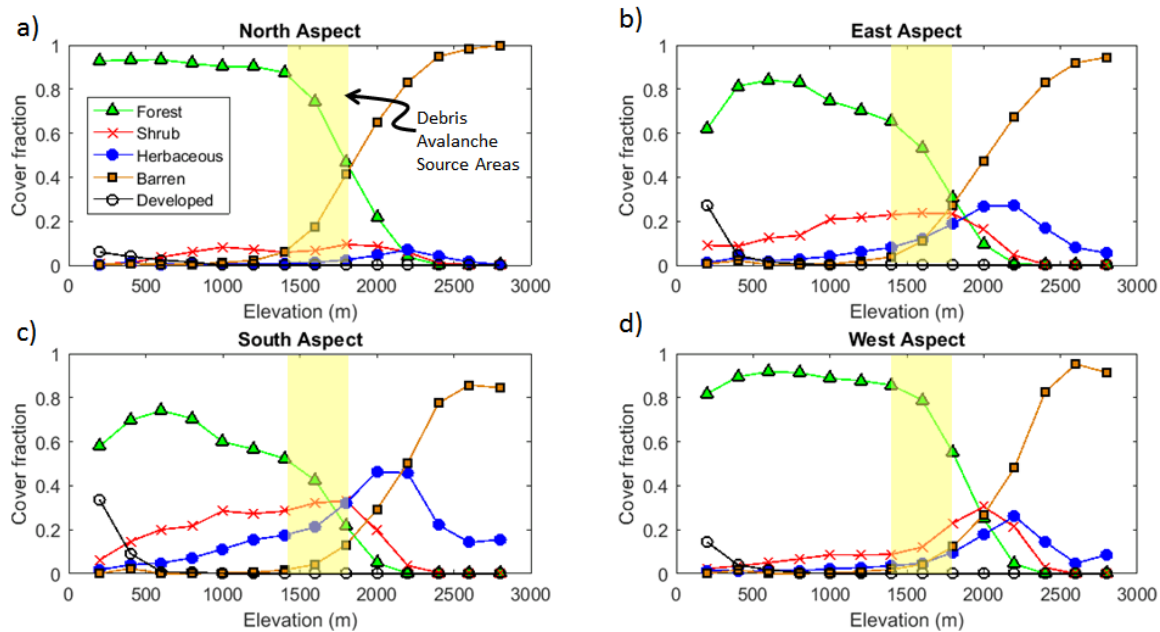
20
21 **Figure 5.** Vegetation cover fraction in NOCA on each aspect, taken as the fraction of vegetation type
22 within each 200-m elevation band. Aspects categorized here as **a)** north (0° to 45° and 315° to 360°), **b)**
23 east (45° to 135°), **c)** south (135° to 225°), and **d)** west (225° to 315°), covering 23%, 23%, 26%, and
24 28% of NOCA, respectively. Yellow highlighted area represents the strongest elevation association for
25 debris avalanche source areas.

26 When all landslides are considered, northern slopes exhibit growing landslide association while
27 landslide frequency declines in southeastern slopes compared to the other landslide datasets (Fig.
28 4a, b). North-facing slopes have been documented to retain more soil moisture than south-facing
29 aspects in northern latitudes (Geroy et al., 2011), which can be broadly responsible for more

initiation, transport and deposition impact of all mass wasting types. Hillslope asymmetry (i.e., steeper slopes depending on aspect) was not found during inspection of average slope on the four primary aspects. North-south asymmetry has been found to demonstrate reversal based on elevation and at 49° latitude, which correspond to the northern edge of NOCA (Poulos et al., 2012). In general, the relatively similar aspect associations for different landslide observation datasets likely indicates the connection of source areas to downstream processes of transport and deposition (Fig. 1).

Comparisons among all landslides, whole debris avalanches, and debris avalanche source areas clearly show that unconsolidated sediments, largely derived from transport and depositional processes, have stronger association with landslides than other lithologies followed by sedimentary rock (Fig. 4). This strong association is expected given the inclusion of mass wasting landforms in the classification of unconsolidated sediment. The high ultramafic rock association when considering all landslide types is driven by a single topple/fall occurring in this scarce lithology (<0.02% of NOCA). Widespread observation of debris avalanche source areas in all rock types may point to the role of steep slopes regardless of lithology. For debris avalanche processes, sedimentary rock is more associated with transport and depositional areas than source areas. Areas without landslide activity were associated with weak metamorphic foliated and intrusive igneous lithology (Fig. 4a).

The association of landslides on concave/converging versus convex/diverging topography is relatively consistent among the datasets and generally consistent with literature due to enhanced wetness where vegetative support may be weak in deeper soils (see Hales et al., 2009; Fig. 4). High wetness index is associated with landslides for all landslide types as well as entire debris avalanches (Fig. 4a,b). This result is intuitive as this index is an indicator of increased soil saturation and surface runoff. In contrast, source areas were correlated with low wetness index (Fig. 4c). This counterintuitive finding, however, aligns with previously discussed results that source areas are associated with loss of root strength, steep slopes and higher elevations, resulting in relatively small specific catchment areas. By definition, wetness index is negatively correlated with slope and positively correlated with specific contributing area. Thus, source areas will have a low wetness index when they are from steep slopes with small contributing areas (i.e., located higher up on hillslopes).

3.2 Susceptibility Index
A susceptibility index (SI) is calculated for each grid cell within the study area domain by equation (3). Cumulative distributions for SI, plotted as fraction of area of the study domain as well as only in the areas where landslide impact was mapped show higher SI values for a given fraction of the respective domains where a given SI is exceeded (Fig. 6a, d, and g). Additional support beyond the graphics that these distributions are not equal is provided by the Kolmogorov-Smirnov test, which rejects the null hypothesis of equal distributions at $\alpha<0.01$. The cumulative distributions show that the SI calculated from FR method can differentiate mapped landslide locations from non-landslides with a larger SI. The resulting spatial distribution of SI is right skewed as shown in the relative frequencies of SI for all three landslide datasets (Fig. 6b, e, and h). The right skew indicates that there is a small population of grid cells with high SI compared to the majority of grid cells in the study domain. This occurs when there are FR

1 subcategories frequently associated with landslides coinciding at the same location. Histograms
2 show a greater relative frequency of landslide grid cells with high SI values than the entire
3 domain (Fig. 6b, e, and h). For source areas, SI bins for the histograms were larger (e.g., 0.5 vs
4 0.25) due to the small number of source area cells compared to the two other datasets.
5
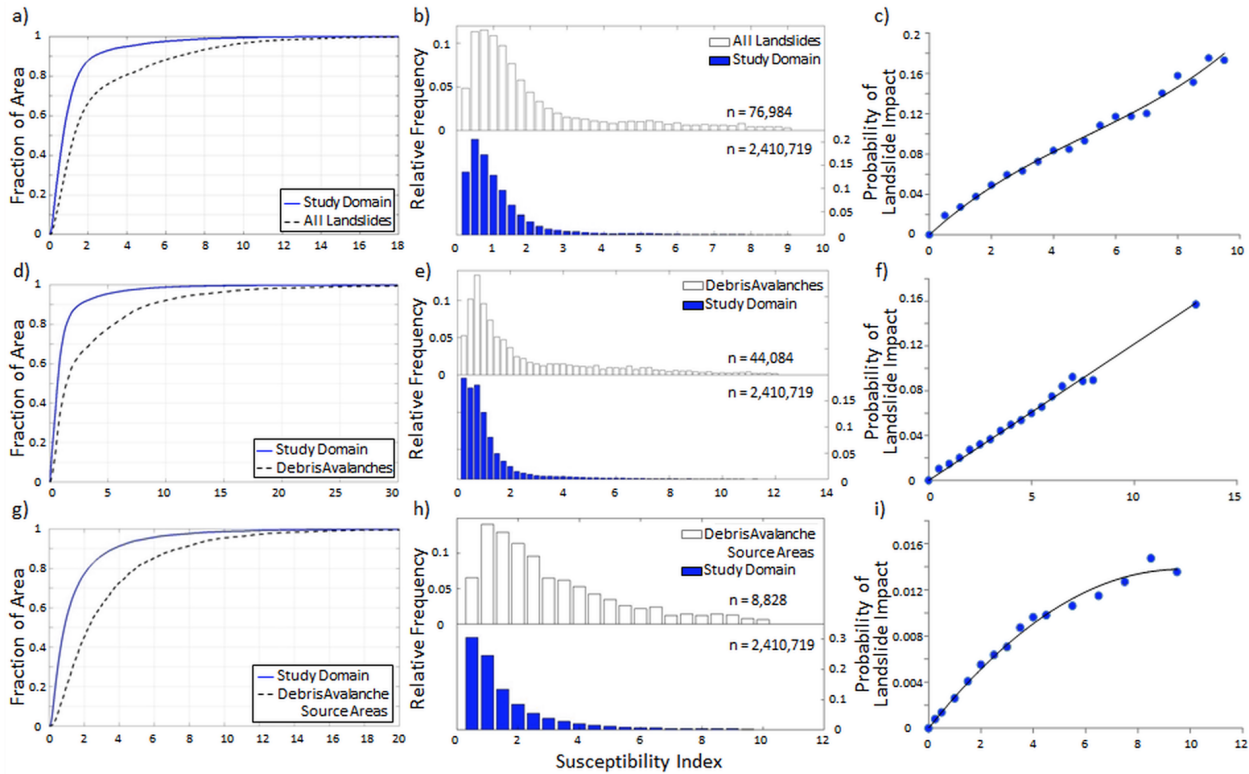
6
7 **Figure 6.** Cumulative distributions *(a, d, and g - column 1)* and relative frequency plots *(b, e, and h -*
8 *column 2)* of Susceptibility Index (SI) for *all* grid cells included in the analysis and the grid cells
9 contained within mapped landslides. *Third column* (**c, f,** and **i**) is the probability of landslide impact,
10 $P(LS_r|SI_r)$, calculated from the ratio of the number of landslide cells to the number of all cells with each
11 SI bins with fitted curves. *Rows* represent analysis domains: **a, b,** and **c)** all landslide types; **d, e,** and **f)**
12 debris avalanches; and **g, h, and i)** debris avalanche source areas.

13 The probability of landslide impact, $P(LS_r|SI_r)$, calculated from Eq. (4) are shown in the third
14 column of Figure 6 (Fig. 6c, f, and i). In calculating this probability in the highest SI bins (e.g.,
15 SI$\geq$8), landslide sample sizes of about 500 or fewer were aggregated into the previous bin. In all
16 three cases, $P(LS_r|SI_r)$ increases with SI, supporting the statistical power of this empirical
17 approach. The SI to $P(LS_r|SI_r)$ relation is explained by a linear function when debris avalanche
18 data are used (Fig. 6f). The other two cases, all landslide data and debris avalanche source areas,
19 are better represented by polynomial fits (Fig. 6c and i). The range of probabilities grows with
20 the sample size of the landslide dataset used, leading to maximum probabilities of 0.2, 0.16, and
21 0.017 for all landslide, debris avalanches, and debris avalanche source areas, respectively. These
22 functions were used to develop continuous empirical probability maps based on SI values
23 assigned to each grid cell of the study domain, limited to the maximum empirical probability of
24 each landslide type.
25

18

1 3.3 Landslide Hazard Maps
2 The probability of landslide impact estimated from SI, P(LS$_r$|SI$_r$), declines as the amount of
3 observational information decreases from all landslides (Fig. 7a), to debris avalanches (Fig. 7b),
4 and debris avalanche source areas (Fig. 7c). This pattern reflects the smaller area of observed
5 landslide data used in each case compared to the study domain. Additionally, the probability of
6 any landslide activity would be expected to be higher than the probability of initiating a debris
7 avalanche alone. When considering all landslides, the highest probabilities are located near the
8 base of valley walls and in topographic depressions or hollows (Fig. 7a). The hazard map
9 developed from the empirical model using only debris avalanches (Fig 7b) also shows higher
10 probabilities in the valley bottoms, but lower probabilities than the all landslides map at higher
11 elevations in alpine areas where the footprint of debris avalanches is smaller compared to the
12 deposition area, reducing the overall probabilities in the FR approach. Spatial patterns of
13 landslide probabilities obtained from the source areas of debris avalanches (Fig. 7c) depart from
14 the other two empirical models with the highest probabilities in middle and upper portions of
15 valley walls, similar to the process model (Fig. 8b). Thus, the empirically-based modeling using
16 only source areas appears to capture some of the physical processes initiating debris avalanches.
17 Closeup areas mapped for each mapping case more clearly illustrate the landslide hazard in
18 relation to topographic position.
19
20 We developed a map of annual probability of shallow landslide initiation by combining the
21 empirical SI-based probability (Fig 7c) and the physically-based annual probability of landslide
22 initiation from Strauch et al. (2018), $P(FS_c \leq 1)$, using the methodology developed in this paper
23 (Eq. 8 and 9). The weight term, $P(FS_c \leq 1)$, and the P(LS) are shown in Fig. 8. Close ups of
24 three locations are shown below the full NOCA maps.
25
26 Approximately 30% of the analyzed cells had weights > 1. Weights are greater in high elevations
27 and steep slopes, commensurate with debris avalanche source areas. Overall 88% of the NOCA
28 area has less than annual landsliding probability of 0.1 in $P(FS_c \leq 1)$ and P(LS) map. P(LS)
29 map (Fig. 8c and f) shows enhanced landslide probability in areas already modeled as high
30 probability of landslide impacts based on the physically-based shallow landslide model (Fig. 8b
31 and e). An anomaly map created by subtracting P(LS) from $P(FS_c \leq 1)$ provides easier display
32 of the effect of the empirical adjustment. In the anomaly map, much of the original $P(FS_c \leq 1)$
33 is adjusted by less than ±0.1 (Fig. 9). East-facing aspect, concave curvature, and elevations in
34 the ~1,000 to 1,600 m range show an increase in probability > 0.1 (Fig. 9). Increasing
35 probabilities on east-facing slopes compared to other aspects aligns with the FR findings (Fig. 4).
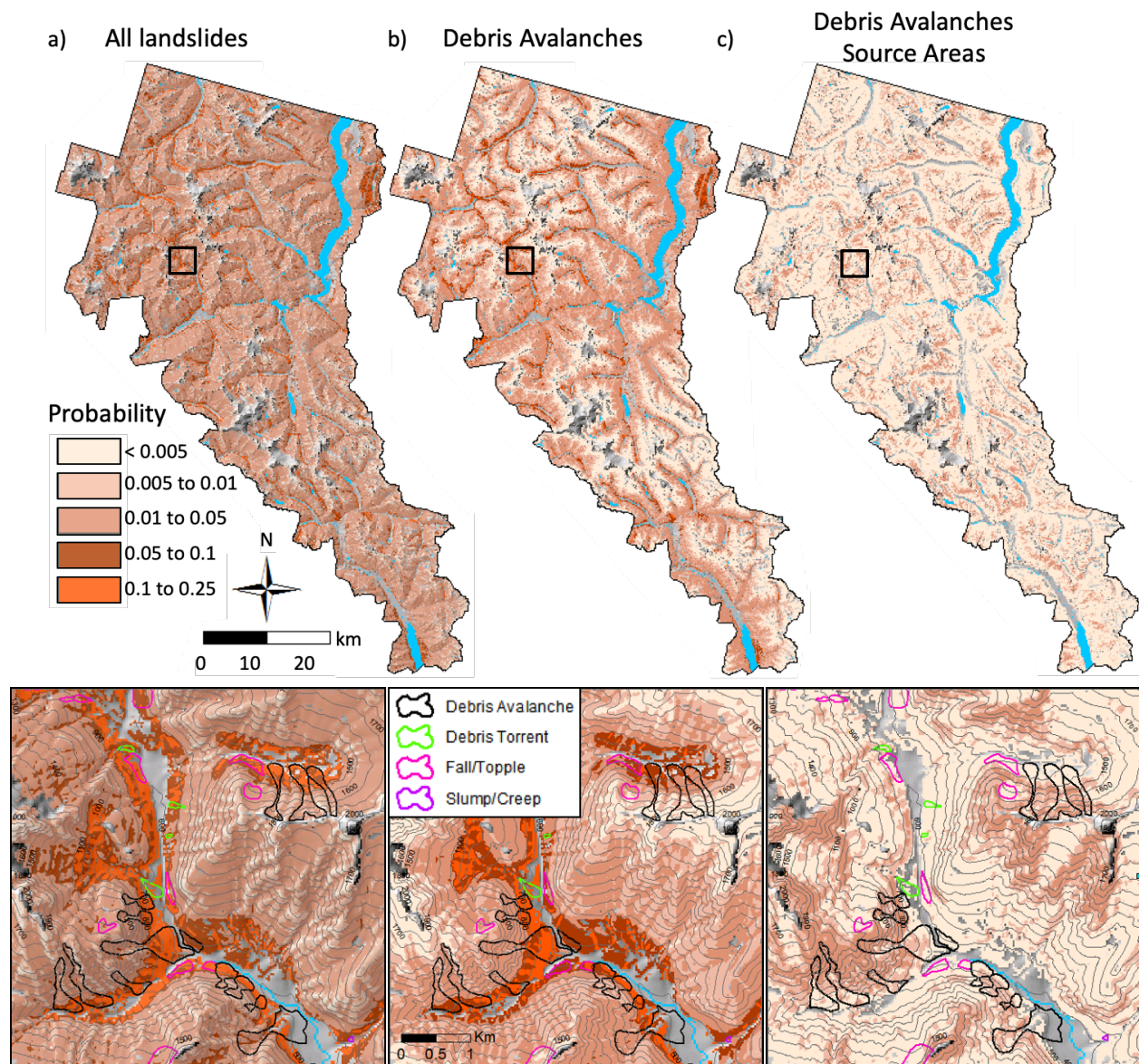36

Figure 7. Maps of probability of landslide impact derived from empirical model based on: **a)** all landslide types, **b)** debris avalanches, and **c)** and source areas of debris avalanches overlain on hillshade raster. Black boxes indicate closeup areas shown below with overlain landslide types and 100 m contours. Gray areas excluded from analysis show river valleys and glaciated crests.
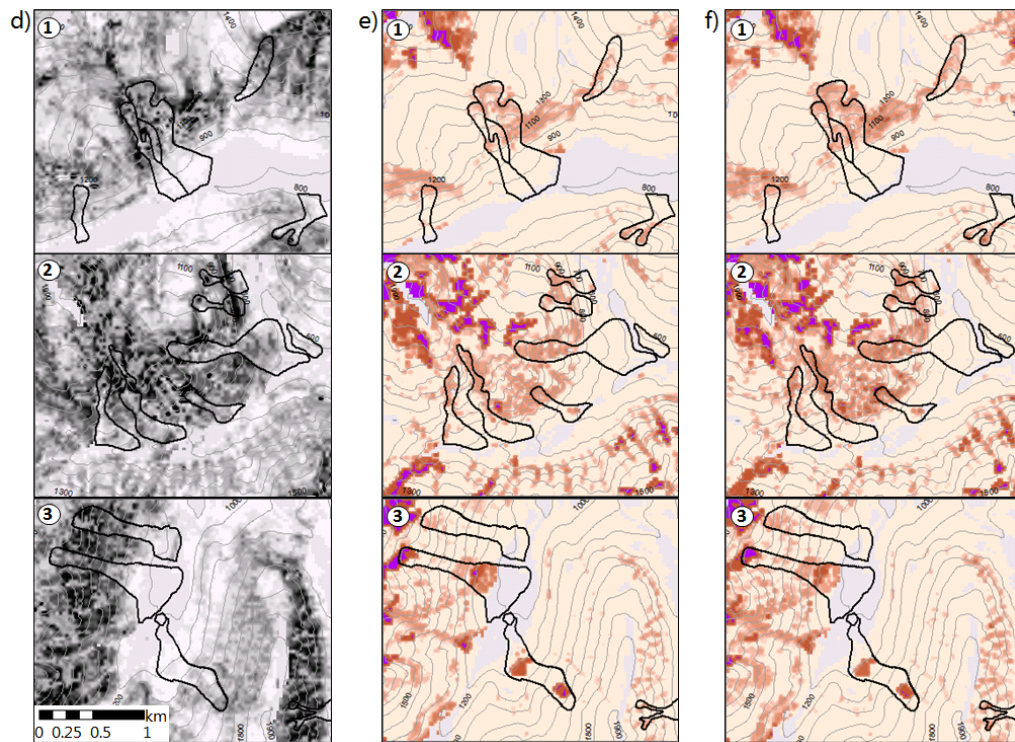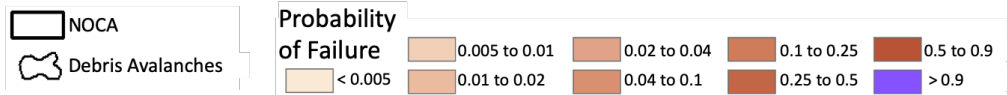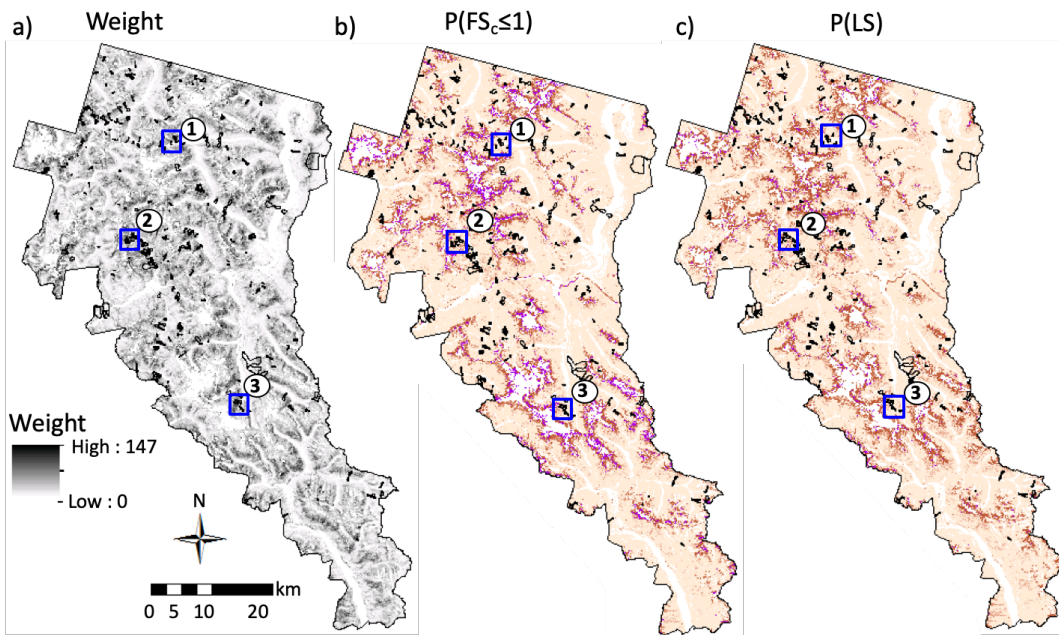
a) Weight   b) P(FS$_c$≤1)   c) P(LS)

Weight
High : 147

- Low : 0

N

km
0 5 10   20

NOCA

Debris Avalanches

Probability
of Failure
< 0.005	0.005 to 0.01	0.02 to 0.04	0.1 to 0.25	0.5 to 0.9
	0.01 to 0.02	0.04 to 0.1	0.25 to 0.5	> 0.9

d) e) f)

① ② ③

km
0 0.25 0.5   1

Figure 8. Maps of: **a)** weight term derived from joint empirical and physically-based modeled probabilities, **b)** $P(FS_c \leq 1)$ from Strauch et al. (2018), and **c)** P(LS) created from multiplying a) by b) at each grid cell for the North Cascades National Park Complex (NOCA). Blue boxes indicate three closeup locations shown below in **d)**, **e)**, and **f)**. Black lines show mapped debris flow boundaries. Gray areas are excluded from analysis and contours are at 100 m.

Other cells declined in probability, particularly on gentler slopes, north to west-facing aspects, and at low (< 1000 m) and high (>1,600 m) elevations (Fig. 9). Areas with reduced probability high on the mountain, above the elevation limit of vegetation (~2,200 m, Fig. 5) and just below actively receding glaciers or permanent snowfields, likely represent limited soil development and active surface erosion where slopes are steep (Roering et al., 2003) (Fig. 9). Within the elevation range of the park, debris avalanche initiation is not frequently observed at the highest elevations where soil is thin or the landscape is covered seasonally by snow and ice.
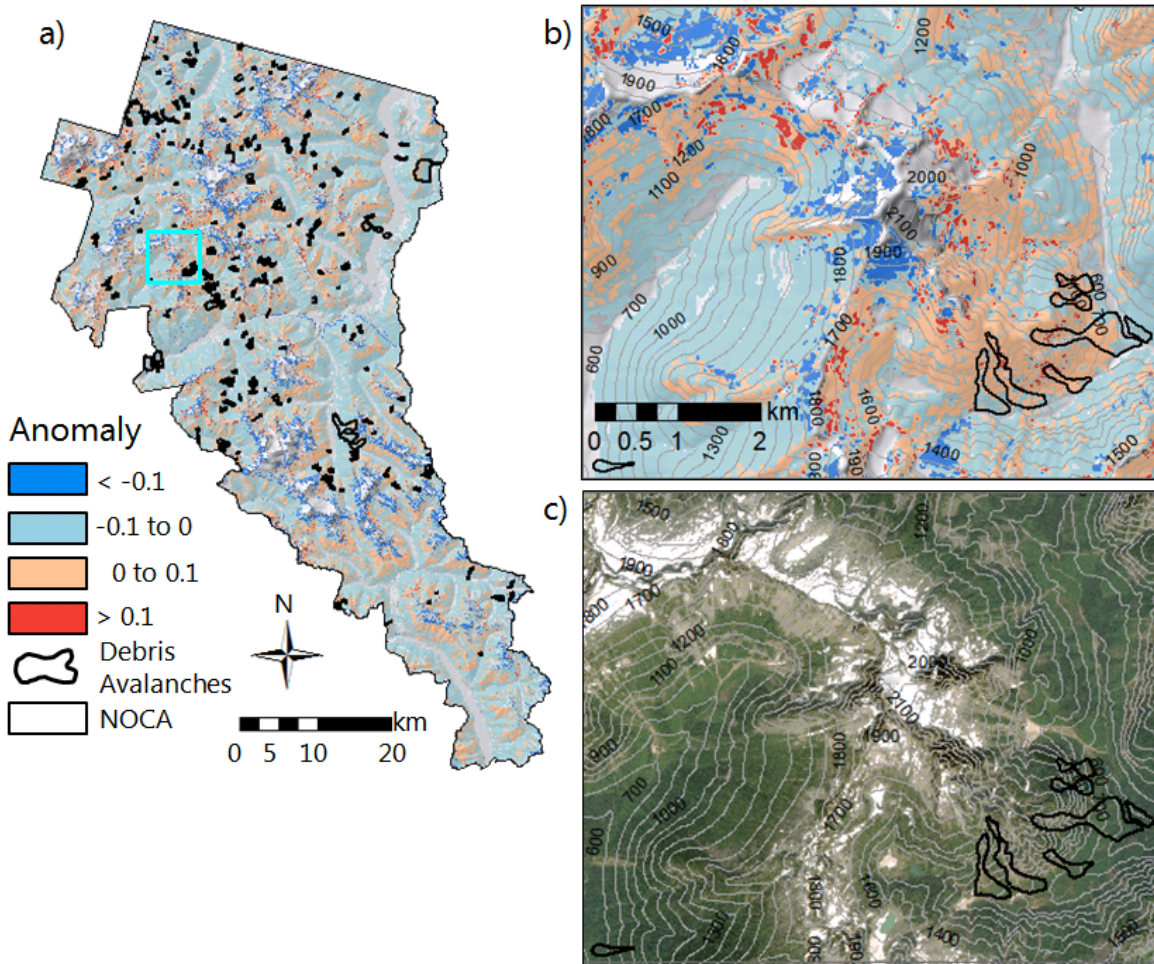

Figure 9. Anomaly maps displaying the difference between *P(LS)* and $P(FS_c \leq 1)$ where blues represent > 0.1 reduction in probability and reds represent > 0.1 increase in probability due to the empirical adjustment. Maps of: **a)** the entire North Cascades National Park Complex, **b)** closeup location indicated by cyan box in a) overlain on hillshade raster, and **c)** aerial image of the same location as b). Aerial image is from World Imagery, Esri Inc. (images created using ArcGIS® software by Esri. ArcGIS® and ArcMap™ are the intellectual property of Esri and are used herein under license. Copyright

To investigate the spatial distribution of $P(FS_c \leq 1)$ (Strauch et al., 2018) and empirically-adjusted model probabilities, P(LS), we plot the cumulative distributions of probabilities (Fig. 10a). In roughly 15% of the NOCA domain, P(LS) gives lower landslide probability than $P(FS_c \leq 1)$, indicated by the upward shift in the cumulative distribution (blue line) (Fig. 10a). The modeled landscapes have P(Failure) ≥ 0.9, or recurrence interval ≤ 1.1 year, in ~6% and ~3% for $P(FS_c \leq 1)$ and P(LS) models, respectively (Fig. 10a). These cells represent highly unstable slopes and the empirical adjustment reduced this area by half from the physically-based model. Unconditionally unstable landslide, P(Failure)=1 (Pack et al., 1998; Montgomery, 2001, corresponds to 0% and 2% of $P(FS_c \leq 1)$ and P(LS) models, respectively. Unconditionally stable slopes, P(Failure)=0, corresponds to 49% of the study domain for both $P(FS_c \leq 1)$ and P(LS) models (not visible in Fig. 10a). The distributions generally show a high portion (~87 to 88%) of the modeled landscapes has P(Failure) ≤ 0.1, or a return period of ≥ 10 years. Only between 7% and 9% of the landscape has a wide range of potential failure ($0.1 \leq$ P(Failure) ≤ 0.9) as indicated by the shaded blue (Fig. 10a), where empirical evidence enhanced the local landscape susceptibility to initiation of shallow landslides.
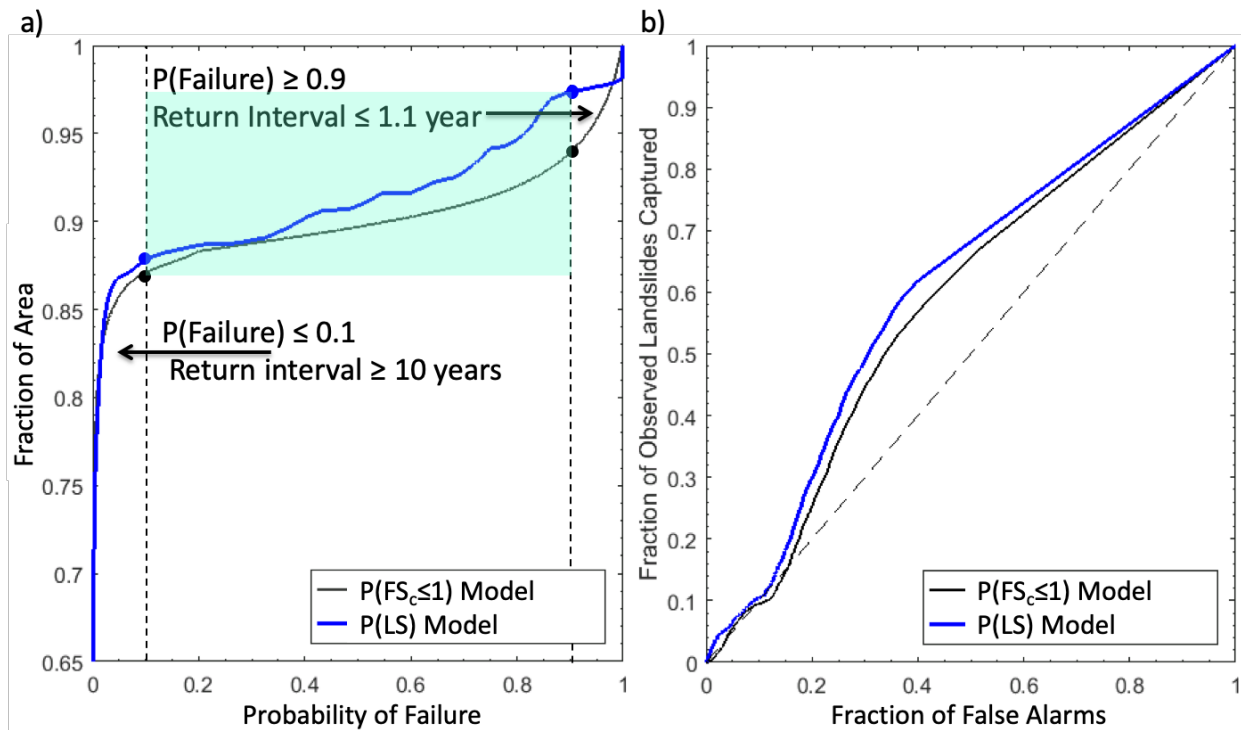

Figure 10. a) Cumulative distribution of the probability of failure for the $P(FS_c \leq 1)$ [black] and P(LS) [blue] using only debris avalanche source areas, **b)** ROC curves for the same two datasets. The blue shaded area on a) represents the fraction of the landscape with $0.1 \leq$ P(Failure) ≤ 0.9. Black diagonal dashed line on a 1 : 1 line in b) represents the case of a trivial or random classification model. AUC values are 0.58 for the modeled probability and 0.60 for the integrated probability.

We anticipated that the additional consideration of the empirical model represented by the weighting term improves the performance of the purely physically-based model. Thus, to assess the potential performance of the models, we statistically evaluated the models using the receiver operating characteristics (ROC) curves (Fawcett, 2006). This approach examines cells within mapped landslides and cells outside landslides for a study area and compares this to randomly distributed landslides over the same landscape. Confusion matrices are generated from observed and modeled landslides based on varying the probability of a landslide threshold used to generate ROC curves (Mancini, et al., 2010; El-Ramly et al., 2002; Anagnostopoulos et al., 2015) (Fig. 10b). A better-performing model curves towards the upper left corner, and a curve along the 1:1 line represents a trivial model that randomly assigns landslide and non-landslide cells. The area under the curve (AUC) statistic provides a numerical indicator of model performance representing the probability of correctly assigning two randomly selected cells to landslide and non-landslide datasets (Hanley and McNeil, 1982).

Both the physically-based model, $P(FS_c \leq 1)$, and the P(LS) perform better than a trivial model by plotting the ROC curve above the 1:1 line (Fig. 10b). The AUC statistic was 0.58 and 0.60 for $P(FS_c \leq 1)$ and P(LS), respectively. The ROC and AUC indicate an improvement in the fraction of observed landslides captured by P(LS) over $P(FS_c \leq 1)$. The AUC for P(LS) indicates that there is a 60% chance that the proposed empirical adjustment to the physically-based model would classify a landslide initiation cell and a non-landslide cell correctly from two randomly sampled grid cells. The ROC analysis found that the optimum probability threshold for maximizing the observed landslides captured and minimizing false alarms was a probability threshold of 0.0006 (i.e., apex of the blue curve); thresholds less than this increased the false alarms and thresholds greater than this reduced the accuracy of capturing observed landslides (Fig. 10b). The additional information from empirical modeling modestly improved the physically-based model and indicates empirical evidence on landslides can capture mechanisms lacking in the infinite slope stability model. These include clustering of debris avalanches due to variability in the bedrock geology (e.g. hydrothermal alteration, steeply dipping bedding planes, and glacial oversteepening). Additional validation approaches, such as separating landslide data into training and testing datasets, may yield additional findings that are deferred to future studies.

4 Conclusions

Empirically-based probability hazard maps were developed from a statistically-based susceptibility index, which integrated the influence of site attributes on observed landslides based on a frequency ratio approach. Resulting susceptibility depends on the observations of landslides considered: all types of landslides, debris avalanches only, or source areas of debris avalanches. Thus, the objectives of a hazard identification study dictate the necessary inventory of landslide features. The empirically-based probability model based on source areas was used to adjust a previously developed physically-based probabilistic model through a calculated weighting term developed from a joint spatial probability. The frequency analysis, hazard map development, and integrated probability model identified several key findings when applied to a national park:

- Frequency analysis shows a clear and growing control of local slopes greater than 35° on landslide initiation, while higher landslide hazard at gentler slopes (<30°) reflects transport and depositional processes.
- Debris avalanche source areas are associated with mid to high elevation (1,400 to 1,800 m), while all landslides types and whole debris avalanches have growing impact in lower elevations (< 1,200 m) with the highest impact falling in elevations <400 m.
- Slope is a key attribute for the initiation of landslides, while lithology is mainly tied to transport and depositional processes.
- The transition from subalpine to alpine herbaceous vegetation with lower root cohesion correlates with higher frequency of debris avalanche initiation.
- East (west) aspect is a positive (negative) landslide-influencing factor, likely due to differences in moisture regime, and forest cover and associated root cohesion.
- Empirical statistical modeling used to adjust a physically-based model of landslide initiation improved predictability of observed landslides by accounting for additional factors that influence the landscape susceptibility to failure not represented in the physically-based model.
- Empirical adjustments generally lowered the probability of failure of the physically-based model, especially for $0.1 \leq P(failure) \leq 0.9$ that covered between 7 to 9% of the study area.

As the occurrence of landslide runout is conditioned on the failure of source areas, future studies could combine the probabilistic initiation methodology we propose in this paper with a landslide runout model to improve prediction of hazards from entire landslides. The applicability of our approach to characterize shallow landslides hazard is limited by the quality of the site-specific data on soils and vegetation, extent of hydrologic modeling, as well as the accuracy and completeness of the landslide inventory. Accurate data for environmental variables such as geology, soils, and vegetation would be as important as comprehensive landslide data as the empirical approach relates landslide hazard to the environmental variables. Although the approach is applicable elsewhere, our results from the empirical analyses are specific to the region in which they were developed and may differ in another location with different geology and landslide inventories. Additionally, the probabilities are likely to change as local conditions change from disturbance such as fire or as climate continues to change. Advancements in surface terrain delineation and in distributed hydrologic modeling specifically contribute to the broad applicability of this approach. We provide multiple landslide hazard maps for the national park that land managers can use for planning and decision making, as well as educating the public about hazards from landslides so they can minimize risks from these geohazards.

Author contributions. RS and EI designed the research, developed the models, performed the simulations, and created figures. JR provided landslide and geology data as well as insights on the approach and model demonstration. RS prepared the manuscript with contributions from all co-authors.

References

Agee, J. K., and Kertis, J.: Forest types of the north Cascades National Park Service complex. Can. J. Botany, 65(7), 1520-1530, 1987.

Aleotti, P. and Chowdhury, R.: Landslide hazard assessment: summary review and new perspectives. Bulletin of Engineering Geology and the environment, 58(1), 21-44 pp., 1999.

Anagnostopoulos, G. G., Fatichi, S., and Burlando, P.: An advanced process-based distributed model for the investigation of rainfall-induced landslides: The effect of process representation and boundary conditions. Water Resour. Res., 51(9), 7501-7523, 2015.

Ayalew, L., Yamagishi, H., and Ugawa, N.: Landslide susceptibility mapping using GIS-based weighted linear combination, the case in Tsugawa area of Agano River, Niigata Prefecture, Japan. Landslides, 1(1): 73-81, 2004.

Baum, R.L., Galloway, D.L., and Harp, E.L.: Landslide and land subsidence hazards to pipelines: U.S. Geological Survey Open-File Report 2008-1164, 192 pp., 2008.

Beaty, C.B.: Landslides and Slope Exposure. J. Geol., 64:1, 1956.

Bellugi, D., Milledge, D.G., Dietrich, W.E., Perron, J.T., and McKean, J.: Predicting shallow landslide size and location across a natural landscape: Application of a spectral clustering search algorithm. J. Geophys. Res.-Earth, 120(12): 2552-2585, 2015.

Beven, K. J., and Kirkby, M. J.: A physically based, variable contributing area model of basin hydrology. Hydrolog. Sci. J., 24(1): 43-69, 1979.

Bordoni, M., Meisina, C., Valentino, R., Bittelli, M., and Chersich, S.: Site-specific to local-scale shallow landslides triggering zones assessment using TRIGRS, Nat. Hazard. Earth Sys., 15(5): 1025-1050, 2015.

Borga, M., Fontana, G.D., and Cazorzi, F.: Analysis of topographic and climatic control on rainfall-triggered shallow landsliding using a quasi-dynamic wetness index. J. Hydrol., 268(1): 56-71, 2002.

Carrara, A., Cardinali, M., Guzzetti, F., and Reichenback, P.: GIS technology in mapping landslide hazards, in: Geographical Information System in Assessing Natural Hazard, edited by: Carrara, A., and Guzzetti, F., Springer, Dordrecht, 135-175 pp., 1995.

Carson, M. A., and Kirkby, M. J.: Hillslope Form and Process, Cambridge Univ. Press, Cambridge, U.K., 475 pp., 1972.

Cevasco, A., Pepe, G., and Brandolini, P.: The influences of geological and land use settings on shallow landslides triggered by an intense rainfall event in a coastal terraced environment. B. Eng. Geol. Environ., 73(3): 859-875, 2014.

Chalkias, C., Ferentinou, M., and Polykretis, C.: GIS-based landslide susceptibility mapping on the Peloponnese Peninsula, Greece. Geosciences, 4(3), 176-190, 2014.

Chung, C. F., Fabbri, A. G., and Van Western, C. J.: Multivariate regression analysis for landslide hazard zonation, in: Geographical Information System in Assessing Natural Hazard, edited by: Carrara, A. and Guzzetti, F., Springer, Dordrecht, 107–133, 1995.

Coe, J. A.: Landslide hazards and climate change: A perspective from the United States, in: Slope safety preparedness for impact of climate change, Chapter: 14., edited by: Ho, K., Lacasse, S., and Picarelli, L., CRC Press, Boca Raton, FL., 479-523 pp., 2016.

Collins, B. D., and Montgomery, D. R.: The legacy of Pleistocene glaciation and the organization of lowland alluvial process domains in the Puget Sound region. Geomorphology, 126(1): 174-185, 2011.

Corominas, J., Van Westen, C., Frattini, P., Cascini, L., Malet, J. P., Fotopoulou, S., Catani, F., Van Den Eeckhaut, M., Mavrouli, O., Agliardi, F., and Pitilakis, K.: Recommendations for the quantitative analysis of landslide risk. B. Eng. Geol. Environ., 73(2): 209-263, 2014.

Croke, J. C., and Hairsine, P. B.: Sediment delivery in managed forests: a review. Environ. Rev., 14(1), 59-87, 2006.

Crozier, M. J.: Deciphering the effect of climate change on landslide activity: A review. Geomorphology, 124(3): 260-267, 2010.

Dai, F.C., Lee, C.F.: Landslide characteristics and slope instability modeling using GIS, Lantau Island, Hong Kong. Geomorphology 42:213–228, 2002.

Densmore, A.L., Anderson, R.S., McAdoo, B.G., and Ellis, M.A.: Hillslope evolution by bedrock landslides, Science, 275: 369-372, 1997.

El-Ramly, H., Morgenstern, N. R., and Cruden, D. M.: Probabilistic slope stability analysis for practice, Can. Geotech. J., 39, 665–683, 2002.

Ercanoglu, M., and Sonmez, H.: General Trends and New Perspectives on Landslide Mapping and Assessment Methods. In Environmental Information Systems: Concepts, Methodologies, Tools, and Applications, pp. 64-93. IGI Global, 2019.

Evans, R. D., and Fonda, R. W.: The influence of snow on subalpine meadow community pattern, North Cascades, Washington. Can. J. Botany, 68(1): 212-220, 1990.

Fawcett, T.: An introduction to ROC analysis, Pattern Recogn. Lett., 27(8):861-874, 2006.

Fischer, L., Kääb, A., Huggel, C., and Noetzli, J.: Geology, glacier retreat and permafrost degradation as controlling factors of slope instabilities in a high-mountain rock wall: the Monte Rosa east face. Nat. Hazard. Earth Sys., 6(5): 761-772, 2006.

Gabet, E. J.: Sediment transport by dry ravel. J. Geophys. Res.-Sol. Ea., 108(B1), 2003.

Geroy, I. J., Gribb, M. M. Marshall, H. P. Chandler, D. G. Benner, S. G. and McNamara, J. P.: Aspect influences on soil water retention and storage. Hydrol. Process., 25, 3836–3842, doi:10.1002/hyp.8281, 2011.

Ghirotti, M.: The 1963 Vaiont landslide, Italy, in: Landslides: Types, mechanisms and modeling, edited by: Claque, J. J. and Stead, D. Cambridge University Press, NY., 359 pp, 2012.

Gokceoglu, C., Sonmez, H., Nefeslioglu, H. A., Duman, T. Y., and Can, T.: The 17 March 2005 Kuzulu landslide (Sivas, Turkey) and landslide-susceptibility map of its near vicinity. Eng. Geol., 81(1): 65-83, 2005.

Gupta, R. P., and Joshi, B. C.: Landslide hazard zoning using the GIS approach—a case study from the Ramganga catchment, Himalayas. Eng .Geol., 28(1): 119-131, 1990.

Haeberli, W., Schaub, Y., Huggel, C.: Increasing risks related to landslides from degrading permafrost into new lakes in de-glaciating mountain ranges. Geomorphology: https://doi.org/10.1016/j.geomorph.2016.02.009, 2016.

Hales, T. C., Ford, C. R., Hwang, T., Vose, J. M., and Band, L. E.: Topographic and ecologic controls on root reinforcement, J. Geophys. Res., 114, F03013, doi:10.1029/2008JF001168, 2009.

Hamlet, A. F., Elsner, M. M., Mauger, G., Lee, S., and Tohver, I.: An Overview of the Columbia Basin Climate Change Scenarios Project: Approach, Methods, and Summary of Key Results, Atmos. Ocean., 51, 392–415, 2013.

Hanley, J. A. and McNeil, B. J.: The meaning and use of the area under a receiver operating characteristic (ROC) curve, Radiology, 143, 29–36, 1982.

Haugerud, R.A., and Tabor, R.W.: Geologic map of the North Cascade Range, Washington, US Department of the Interior, U.S. Geological Survey, 29 pp., 2009.

Hobley, D. E. J., Adams, J. M., Nudurupati, S. S., Hutton, E. W. H., Gasparini, N. M., Istanbulluoglu, E., and Tucker, G. E.: Creative computing with Landlab: an open-source toolkit for building,

coupling, and exploring two-dimensional numerical models of Earth-surface dynamics, Earth Surf. Dynam., 5, 21–46, https://doi.org/10.5194/esurf-5-21-2017, 2017.

Hong, H., Chen, W., Xu, C., Youssef, A. M., Pradhan, B., and Tien Bui, D.: Rainfall-induced landslide susceptibility assessment at the Chongren area (China) using frequency ratio, certainty factor, and index of entropy. Geocarto Int., 32(2): 139-154, 2017.

Hungr, O., Leroueil, S., and Picarelli, L.: The Varnes classification of landslide types, an update. Landslides, 11(2): 167-194, 2014.

Hungr, O.: A review of landslide hazard and risk assessment methodology, in Landslides and engineered slopes. Experience, theory and practice, edited by: Aversa, S., Cascini, L., Picarelli, L., and Scavia, C., CRC Press, Boca Raton, FL, pp. 3-27 pp., 2018.

Jin, S, Yang L, Danielson P, Homer C, Fry J, and Xian, G.: A comprehensive change detection method for updating the National Land Cover Database to circa 2011, Remote Sens. Environ., 132: 159 175, 2013.

Kelsey, H.M.: Formation of inner gorges, Catena, 1 5: 433-458, 1988.

Kirschbaum, D.B., Adler, R., Hong, Y., Kumar, S., Peters-Lidard, C., and Lerner-Lam, A.: Advances in landslide nowcasting: evaluation of global and regional modeling approach. Environ. Earth. Sci., 66: 1683-1696, 2012.

LaHusen, S. R., Duvall, A. R., Booth, A. M., and Montgomery, D. R.: Surface roughness dating of long-runout landslides near Oso, Washington (USA), reveals persistent postglacial hillslope instability. Geology, 44(2): 111-114, 2016.

Lee S., Pradhan, B.: Landslide hazard mapping at Selangor, Malaysia using frequency ratio and logistic regression models. Landslides, 4:33–41, 2007.

Lee, S., Ryu J. H., Kim, I. S.: Landslide susceptibility analysis and its verification using likelihood ratio, logistic regression, and artificial neural network models: Case study of Youngin, Korea. Landslides, 4:327–338, 2007.

Lepore, C., Kamal, S. A., Shanahan, P., and Bras, R. L.: Rainfall-induced landslide susceptibility zonation of Puerto Rico. Environ. Earth Sci., 66(6): 1667-1681, 2012.

Liang, X., Lettenmaier, D. P.,Wood, E. F., and Burges, S. J.: A simple hydrologically based model of land surface water and energy fluxes for GSMs, J. Geophys. Res., 99, 14415–14428, 1994.

Mancini, F., Ceppi, C., and Ritrovato, G.: GIS and statistical analysis for landslide susceptibility mapping in the Daunia area, Italy, Nat. Hazard. Earth Sys., 10(9): 1851, 2010.

May, C.L., Pryor, B., Lisle, T.E., Lang, M.: Coupling hydrodynamic modeling and empirical measures of bed mobility to predict the risk of scour and fill of salmon redds in a large regulated river. Water Resour. Res. 45: W05402, 2009.

Megahan, W.F., Day, N.F., and Bliss, T. M.: Landslide occurrence in the western and central Northern Rocky Mountain physiographic province in Idaho, in Forest Soils and Land Use: Proceedings of the Fifth North American Forest Soils Conference, edited by: Youngberg, C.T., CSU, Ft. Collins, CO, 116-139 pp., 1978.

Miller, D. J., and Burnett, K. M.: Effects of forest cover, topography, and sampling extent on the measured density of shallow, translational landslides: Water Resour. Res., v. 43, no. W03433, 2007.

Montgomery, D. R.: Road surface drainage, channel initiation, and slope instability. Water Resour. Res., 30(6): 1925-1932, 1994.

Montgomery, D.R.: Slope distributions, threshold hillslopes, and steady-state topography. Am. J. Sci., 301(4-5): 432-454, 2001.

Mustoe, G. E., and Leopold, E. B.: Paleobotanical evidence for the post-Miocene uplift of the Cascade Range. Can. J. Earth Sci. 51(8): 809-824, 2014.

O'loughlin, E. M.: Prediction of surface saturation zones in natural catchments by topographic analysis. Water Resour. Res., 22(5): 794-804, 1986.

Pachauri, A. K., and Pant, M.: Landslide hazard mapping based on geological attributes. Eng. Geol., 32(1-2), 81-100, 1992.

Pelto M. S., and Riedel, J.: Spatial and temporal variations in annual balance of North Cascade glaciers, Washington 1984–2000. Hydrol. Process., 15: 3461–3472, 2001.

Pollock, M. M.: Biodiversity, in: River Ecology and Management: Lessons From the Pacific Coastal Ecoregion, edited by: Naiman, R. J., and Bilby, R. E., Springer-Verlag, New York. 430–452 pp., 1998.

Poulos, M. J., Pierce, J. L., Flores, A. N., and Benner, S. G.: Hillslope asymmetry maps reveal widespread, multi-scale organization, Geophys. Res. Lett., 39, L06406, doi:10.1029/2012GL051283, 2012.

Reichenbach, P., Rossi, M., Malamud, B. D., Mihir, M., and Guzzetti, F.: A review of statistically-based landslide susceptibility models. Earth-Science Reviews, 180, 60-91, 2018.

Riedel, J., Dorsch, S., and Wenger, J.: Geomorphology of the Stehekin River watershed: Landform mapping at North Cascades National Park Service Complex, Washington. Natural Resource Technical Report NPS/NCCN/NRTR—2012/566. National Park Service, Fort Collins, Colorado, 90 pp., 2012.

Riedel, J. L., Haugerud, R. A., and Clague, J. J.: Geomorphology of a Cordilleran Ice Sheet drainage network through breached divides in the North Cascades Mountains of Washington and British Columbia. Geomorphology, 91(1-2), 1-18, 2007.

Riedel, J, and Probala, J.: Mapping ecosystems at the landform scale in Washington state, Park Science, 23-2: 37-42, 2005.

Roering, J. J., Schmidt, K. M., Stock, J. D., Dietrich, W. E., and Montgomery, D. R.: Shallow landsliding, root reinforcement, and the spatial distribution of trees in the Oregon Coast Range, Can. Geotech. J., 40, 237–253, 2003.

Roe, G.H.: Orographic Precipitation. Annu. Rev. Earth Planet. Sci., 33:645–71, 2005.

Sidle, R.C., and Ochiai, H.: Landslides: processes, prediction, and land use, Water Resources Monogram 18, American Geophysical Union, Washington DC, 2006.

Strauch, R., Istanbulluoglu, E., Nudurupati, S. S., Bandaragoda, C., Gasparini, N. M., and Tucker, G. E.: A hydro-climatological approach to predicting regional landslide probability using Landlab, Earth Surf. Dynam., 6(1), 49-75. https://doi.org/10.5194/esurf-6-49-2018, 2018.

Swanson, F. J., and Dyrness, C . T .: Impact of clear-cutting and road construction on soil erosion by landslides in the western Cascade Range, Oregon, Geology, 3: 393-396, 1975.

Tabor, R.W., and Haugerud, R.A.: Geology of the North Cascades: a mountain mosaic. The Mountaineers Books, Seattle, WA, 1999.

Taylor, F.A., and Brabb, E.E.: Map showing landslides in California that have caused fatalities or at least $1,000,000 in damages from 1906 to 1984: U.S. Geological Survey Miscellaneous Field Studies Map, MF- 1867, scale: 1:1,000,000, 1986.

United States Department of the Interior, National Park Service (DOI-NPS): Foundation Document, North Cascades National Park Complex, Washington. Available from: https://www.nps.gov/noca/learn/management/upload/North-Cascades-NP-Complex-Foundation-Document_small.pdf, last accessed: 23 January 2017, 2012.

United States Geologic Survey (USGS): National Elevation Data last modified March 6, 2014, National Map Viewer, last accessed: 24 November 2014, 2014a.

USGS: National Land Cover Data (NLCD) version Marched 31, 2014, National Map Viewer, last accessed: 25 November 2014, 2014b.

Van Westen, C.J., Van Asch, T.W., and Soeters, R.: Landslide hazard and risk zonation—why is it still so difficult? B. Eng. Geol. Environ., 65(2): 167-184, 2006.

Wartman, J., Montgomery, D.R., Anderson, S.A., Keaton, J.R., Benoît, J., dela Chapelle, J., and Gilbert, R.: The 22 March 2014 Oso landslide, Washington, USA. Geomorphology, 253: 275-288, 2016.

Washington State Department of Natural Resources (WADNR).: Geologic_unit_poly_100k. Vector digital data, published June 2010. Division of Geology and Earth Resources, Olympia, WA, last accessed: March 27, 2014, 2014.

Wooten, R. M., Witt, A. C., Miniat, C. F., Hales, T. C., and Aldred, J. L.: Frequency and magnitude of selected historical landslide events in the southern Appalachian Highlands of North Carolina and Virginia: relationships to rainfall, geological and ecohydrological controls, and effects, in: Natural Disturbances and Historic Range of Variation, edited by: Greenberg, C. H., and Collins, B. S., Springer International Publishing, Switzerland, 203-262 pp., DOI 10.1007/978-3-319-21527-3, 2016.

Wu, Z., Wu, Y., Yang, Y., Chen, F., Zhang, N., Ke, Y., and Li, W.: A comparative study on the landslide susceptibility mapping using logistic regression and statistical index models. Arab. J. Geosci., 10(8), 187, 2017.